



UNIVERSITÀ POLITECNICA DELLE MARCHE
Repository ISTITUZIONALE

Energy based non-local plasticity models for deformation patterning, localization and fracture

This is the peer reviewed version of the following article:

Original

Energy based non-local plasticity models for deformation patterning, localization and fracture / Lancioni, Giovanni; Yalcinkaya, Tuncay; Cocks, Alan. - In: PROCEEDINGS OF THE ROYAL SOCIETY OF LONDON. SERIES A. - ISSN 1364-5021. - STAMPA. - 471:(2015), pp. 1-23. [10.1098/rspa.2015.0275]

Availability:

This version is available at: 11566/229791 since: 2022-05-27T15:10:07Z

Publisher:

Published

DOI:10.1098/rspa.2015.0275

Terms of use:

The terms and conditions for the reuse of this version of the manuscript are specified in the publishing policy. The use of copyrighted works requires the consent of the rights' holder (author or publisher). Works made available under a Creative Commons license or a Publisher's custom-made license can be used according to the terms and conditions contained therein. See editor's website for further information and terms and conditions.

This item was downloaded from IRIS Università Politecnica delle Marche (<https://iris.univpm.it>). When citing, please refer to the published version.

(Article begins on next page)

Energy based non-local plasticity models for deformation patterning, localization and fracture

Giovanni Lancioni^a, Tuncay Yalçinkaya^{*b,c}, Alan Cocks^b

^a*Department of Civil and building Engineering, and Architecture, Polytechnic University of Marche, Via Brecce Bianche, 60131 Ancona, Italy*

^b*Department of Engineering Science, University of Oxford, Parks Road, Oxford OX1 3PJ, UK*

^c*Department of Aerospace Engineering, Middle East Technical University, 06800, Ankara, Turkey*

Abstract

This paper analyzes the effect of the form of the plastic energy potential on the (heterogeneous) distribution of the deformation field in a simple setting where the key physical aspects of the phenomenon could easily be extracted. This phenomenon is addressed through two different (rate-dependent and rate-independent) non-local plasticity models, by numerically solving two distinct one-dimensional problems where the plastic energy potential has different non-convex contributions leading to patterning of the deformation field in a shear problem, and localization, resulting ultimately in fracture, in a tensile problem. Analytical and numerical solutions provided by the two models are analyzed, and they are compared with experimental observations for certain cases.

Key words: Gradient plasticity, non-convex energy, patterning, softening, localization, fracture

1. Introduction

Recent studies shown that strain gradient plasticity models are able to capture different localization mechanisms such as, deformation patterning leading to plastic anisotropy (see e.g. Yalçinkaya et al. (2011), Yalçinkaya et al. (2012)) and strain localization (Del Piero et al. (2013)) leading to failure of metallic materials through necking, as long as an appropriate non-convex energy is incorporated in a thermodynamically consistent manner. It is observed that during the localization of deformation and evolution of microstructures the macroscopic stress-strain response shows a hardening-softening-stress plateau type of behavior (see e.g. Sun et al. (2003), Yoshida et al. (2008)). The usage of standard finite element methods for this type of problem yields post-critical results due to loss of ellipticity of the incremental boundary value problem (see e.g. de Borst (1987)). Several models have been proposed to remedy these issues including variational regularization methods, non-local methods, viscous regularization techniques, and Cosserat theories. However, models which can fully simulate the realistic patterning of dislocation slip are not

*Corresponding author. Tel. +903122104258 (Tuncay Yalçinkaya)

Email addresses: g.lancioni@univpm.it (Giovanni Lancioni), yalcinka@metu.edu.tr (Tuncay Yalçinkaya), alan.cocks@eng.ox.ac.uk (Alan Cocks)

Preprint submitted Proceedings A

May 27, 2022

available. In order to contribute to understanding in this field, two different approaches are studied here to illustrate the ability of non-convex field models to predict the emergence and the evolution of dislocation slip microstructures and localization leading to failure in both rate-dependent and rate-independent strain gradient settings. The gradient nature of both models not only allows the numerical issues to be regularized (see e.g. de Borst et al. (1995)) but it also gives the opportunity to study processes at different length scales, due to the internal length scale parameter entering the gradient energy contribution. Even though the structure of the non-convex plastic energy functions is not physically based in the current study and based on mathematical concerns, it gives the possibility to control the state of deformation needed for the initiation of patterning and the amount of localized strain, through the spinodal and binodal points of the non-convex plastic energy. This allows direct comparisons with experimental observations, as it is illustrated here for the necking and failure of a steel bar under tensile loading.

The first framework, proposed in Yalcinkaya et al. (2011) and Yalçinkaya et al. (2012), parallels the formulation of strain gradient models developed in Gurtin (2000) and Gurtin (2002), but with additional free energy terms. The dissipation inequality is exploited to obtain the microstress definition, and the plastic evolution equation is obtained to satisfy the reduced dissipation inequality for thermodynamic consistency. It assumes additive decomposition of the free-energy, which consists of a non-convex plastic term, and two quadratic terms with respect to the elastic deformation and the plastic deformation gradient. The resulting rate-dependent model accounts for processes where the plastic deformation is partially recoverable and partially dissipated. In the second framework, developed in Del Piero et al. (2013), and extended in Lancioni (2015), the plastic evolution is determined by incremental minimization of a global energy functional which is equivalent to the free-energy of the previous model. In this case, the plastic term is totally dissipative, and, therefore, plastic deformation is not recoverable. The resulting framework is rate-independent, in contrast to the rate dependency of the previous model. The energy functional considered here has many similarities with the functionals used in variational fracture models (see e.g. the seminal work Bourdin et al. (2000) and the subsequent extensions Del Piero et al. (2007), Amor et al. (2009) and Lancioni and Royer-Carfagni (2009)) and the damage models, such as Freddi and Royer-Carfagni (2010) and Pham et al. (2011). However the proposed functional is different in many respects; the elastic and inelastic terms are totally decoupled, and the elastic properties are not affected by damage parameters. The model presents similarities also with gradient plasticity theories (see Jirásek and Rolshoven (2009a,b) for a review). The main advantage of the proposed variational format, compared to classical plasticity theories, is that, once a proper internal energy is assigned, all the features of plasticity (yield condition, flow rule, consistency condition, etc.) are variationally deduced.

Two different problems are considered through the models above:

(i.) The first problem is the evolution of the heterogeneous plastic deformation (microstructure) in metallic materials. These microstructures may macroscopically manifest themselves through softening or through plastic anisotropy in hardening under strain path changes (see e.g. Yalcinkaya et al. (2009)). The rate-dependent modeling of these phenomena has been studied before (see Yalcinkaya et al. (2011), Klusemann and Yalçinkaya (2013)) through phenomenological double-well potentials. This framework can model the formation and evolution of microstructures including the non-equilibrium stages due to its rate-dependent nature. Incorporation of more physically based

relations for the plastic potential (e.g. non-convex latent hardening potential) has been addressed as well (see e.g. Ortiz and Repetto (1999), Yalçinkaya et al. (2012), Yalcinkaya (2013), Klusemann et al. (2013)). In rate-independent modeling, the relaxation of the associated non-convex incremental variational problem has been the main approach in the literature (see e.g. Miehe and Lambrecht (2003b), Miehe and Lambrecht (2003a)). In most of the cases the non-convexity comes from the finite strain formulation of plasticity (see e.g. Carstensen et al. (2002), Miehe et al. (2004)). A recent study in Klusemann and Kochmann (2014) presents an interesting comparison between the relaxation and gradient plasticity methods in finite plasticity. On the other hand, the current paper addresses the rate-independent evolution of the microstructure without a relaxation step through the incremental minimization of the total energy. The non-convex contribution is a Landau-Devonshire type of double-well functional where the second well is shifted up, similar to the form used in Yalcinkaya et al. (2011). Using such a type of plastic potential results in a Ginzburg-Landau phase-field-like relation for the evolution of plastic slip, where the different phases are identified as regions with high plastic and low plastic strain.

(ii.) The second problem is the material localization, necking and consequent fracture problem in plasticity under uniaxial loading conditions, which is accompanied by substantial softening. The length scale of this problem, which is almost at the engineering level, differs completely from the previous one. In this case, the plastic functional has a convex-concave form, where its concavity is used to simulate the softening phase observed in tensile tests on steel bars. When the amount of plastic deformation reaches values in the concave region strain localization initiates and continues until the material ultimately ruptures. Note that the non-convexity is an intrinsic property of the current models, where the shape of the incorporated plastic potential is designed according to experimental observations. For this problem the response is expressed in terms of nominal quantities so the equations employed here implicitly take into account the effects of both material and geometric softening. The response of steel bars to tensile loadings has recently been studied by using the rate-independent model (see e.g. Lancioni (2015)), and, in the present study, it is solved by the rate-dependent model as well.

The purpose of this work is to demonstrate the influence of the form of the plastic energy function on the inhomogeneous distribution of the deformation field and to prove the ability of the rate-dependent and rate-independent models to capture this phenomenon through numerical examples and by using energy functionals, which has not been considered in previous studies (except the preliminary results in recent conference proceedings Lancioni and Yalcinkaya (2014) and Yalcinkaya and Lancioni (2014)). Furthermore, the proposed study aims at providing an in-depth comparative analysis of the two models. Therefore in order to facilitate the comparison, the two theories are formulated within a common unified framework, which allows immediately to highlight theoretical similarities and differences. In the numerical simulations, a particular attention is paid to the different capabilities of the two models in describing strain localization, considering the rate-dependency and the different nature of the plastic energy (stored or dissipative), and predictive limits and advantages of the two approaches are pointed out. To provide a thorough mechanistic understanding, the derivations and implementation are done in a one-dimensional mathematical setting. The approach can be readily extended to a multi slip strain gradient crystal plasticity setting, or to a three-dimensional isotropic softening gradient plasticity framework.

The paper is organized as follows. First, in Section 2, the problems are summarized in detail,

and the theories of the rate-dependent and rate-independent models are presented. In Section 3, the analytical solutions of the models, determined in a special case, are addressed, with a special focus on the rate-dependent case. Sections 4 and 5 study the numerical results from both models, regarding the two problems described above. Last, in Section 6 the concluding remarks are summarized.

2. Rate-Dependent (RD) and Rate-Independent (RI) models

The basic ingredients of both RD and RI theories are presented here in a unified common framework, which facilitates comparison, highlighting the similarities and the differences of both formulations. We recall the model equations of the RD and RI models, referring to Yalcinkaya et al. (2011) and Del Piero et al. (2013), respectively, for details.

2.1. Problem Statement

Two distinct problems at different length scales described in the introduction, i.e., the microstructure evolution at micro-meso scales and the localization phenomena at the macro scale, are handled separately by both rate-dependent and rate-independent frameworks, where the chosen length scale parameter governs the nature of the problem.

One-dimensional schemes are considered in order to address the phenomena in a more simple way. Regarding the problem of microstructure evolution at micro-meso scales, an infinitely long strip subjected to a shear-strain is considered, as schematically depicted in Fig. 1(a). A single slip system, with shear plane parallel to the slip boundary lines, is considered in such a way that the shear deformation depends only on the x coordinate. Concerning the problem of strain localization and fracture, we consider the problem of a tensile bar described in Fig. 1(c) in terms of nominal quantities. It schematizes the tensile test performed on the bone-shaped sample represented in Fig. 1(b), where the deformation of the enlargements at the extremities are neglected.

Given the one-dimensional domain $(0, l)$ of length l , the displacement of a point $x \in (0, l)$ at the time instant t is denoted by $u = u_t(x)$, where the dependence on time is indicated by a subscript. The boundary conditions are assigned at the endpoints,

$$u_t(0) = 0, \quad u_t(l) = l\varepsilon_t, \quad (1)$$

where ε_t is an imposed positive deformation, function of time. We assume that the deformation is decomposed additively into an elastic part ε^e and a plastic part ε^p . In one-dimensional context of crystal plasticity the plastic strain ε^p basically coincides with the plastic slip γ , and the strain decomposition reads,

$$u' = \varepsilon^e + \gamma. \quad (2)$$

For the analogy with the isotropic gradient plasticity, γ represents the accumulated plastic strain, which coincides with the plastic deformation ε^p if $\varepsilon_t \geq 0$. For an extension of this work to multi-dimension crystal plasticity, plastic strain would be calculated as a sum of plastic slips on different slip systems. Differently, to extend the model to multi-dimension isotropic von Mises plasticity, ε_p would be defined as a purely deviatoric tensor, and the accumulated plastic strain would be $\gamma_t = \sqrt{2/3} \int_0^t |\dot{\varepsilon}_\tau^p| d\tau$. Considering the notation for the derivatives of a given arbitrary function

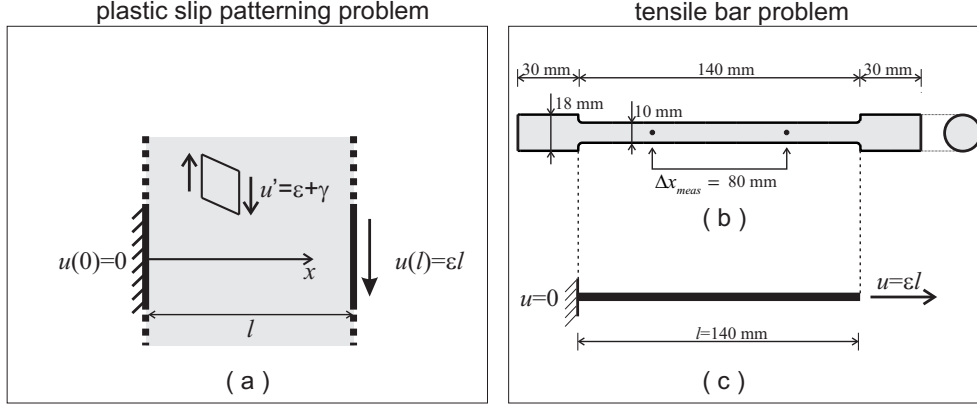


Figure 1: Geometrical schemes of (a) the plastic slip patterning problem, and (b,c) the tensile bar problem.

$v = v_t(w)$, which depends on a certain variable w and on time t , a prime indicates a derivative with respect to w , $v' = dv/dw$, and a dot means a time derivative, $\dot{v} = dv/dt$.

2.2. Constitutive assumptions and models

RD model. The material is assumed to be endowed with a free energy with different contributions according to

$$\psi^{RD}(\varepsilon^e, \gamma, \gamma') = \psi_e(\varepsilon^e) + \psi_\gamma(\gamma) + \psi_{\gamma'}(\gamma'), \quad (3)$$

with elastic, plastic and non-local stored energies respectively. The first term represents the stored energy associated with the stretching of the crystal lattice, while the second and the third terms account for the energy stored in the lattice due to the presence of defects. An analogous additive decomposition was considered in Gurtin and Anand (2009). The elastic and the non-local terms are

$$\psi_e(\varepsilon^e) = \frac{1}{2}E\varepsilon^{e2}, \quad \psi_{\gamma'}(\gamma') = \frac{1}{2}A\gamma'^2, \quad (4)$$

while the plastic potential ψ_γ is a monotonic increasing function of γ . The macroscopic stress and the microscopic hyperstress power-conjugated to ε^e and $\dot{\gamma}'$, respectively, are defined as

$$\sigma = \psi'_e(\varepsilon^e) = E\varepsilon^e, \quad \xi = \psi'_{\gamma'}(\gamma') = A\gamma'. \quad (5)$$

Plastic dissipation is taken into accounts by the viscous micro-stress,

$$\sigma^d = s \left(\frac{|\dot{\gamma}'|}{\dot{\gamma}'_0} \right)^m \text{sign}(\dot{\gamma}'), \quad (6)$$

which establishes a power law relation between the stress terms and the plastic slip rate. Here s is the resistance to dislocation slip, $\dot{\gamma}'_0$ is the reference slip rate and m is the rate sensitivity exponent. In this paper we assume $m = 1$ in order to have a dual formulation with Ginzburg-Landau type phase field models, which would also give a linear drag relation as used in discrete dislocation studies. If we define $c = s/\dot{\gamma}'_0$ as a viscous coefficient, then (6) assumes the simpler form $\sigma^d = c\dot{\gamma}'$.

This assumption, which is absent in the RI model, is the only source of rate-dependency of the model.

RI model. We assume that the free-energy is

$$\psi^{RI}(\varepsilon^e, \gamma') = \psi_e(\varepsilon^e) + \psi_{\gamma'}(\gamma'), \quad (7)$$

where only the first and third term of (3) are considered. The expressions in (4), and the related macroscopic stress and microscopic hyperstress in (5) are still valid here. The plastic energy, which is denoted by $\theta(\gamma)$, is not included in (7), since it is supposed to be totally dissipative. We assume that θ is a monotonic increasing function of γ , equal to ψ_γ of the RD model. It obeys the dissipation inequality

$$\dot{\theta}(\gamma) = \theta'(\gamma)\dot{\gamma} \geq 0, \quad (8)$$

which, under the constitutive assumption $\theta'(\gamma) > 0$, reduces to

$$\dot{\gamma} \geq 0. \quad (9)$$

In the context of isotropic gradient plasticity, γ represents the accumulated plastic strain, therefore the above condition is satisfied by definition (see Lancioni (2015)), and the plastic energy has automatically a dissipative nature. This agrees with the reformulations of the Aifantis theory proposed in Gudmundson (2004) and Gurtin and Anand (2009) in thermodynamically consistent context, according to which the local term of the Aifantis flow rule is dissipative (while the non-local term is energetic). In a multi-slip crystal plasticity setting, the relation (9) becomes $\text{sign}(\gamma_i)\dot{\gamma}_i \geq 0$, with γ_i representing the plastic slip of i -th slip system (see Lancioni et al. (2015) for details).

With these assumptions, the dissipation inequality for isothermal processes

$$D = P - \dot{\psi} \geq 0, \quad (10)$$

with D the local dissipated power and P the local internal power, is automatically satisfied. Indeed, the local internal powers of the RD and RI model are

$$P^{RD} = \dot{\psi}^{RD} + \sigma^d \dot{\gamma} = \sigma \dot{\varepsilon}^e + (\psi'_\gamma + \sigma^d) \dot{\gamma} + \xi \dot{\gamma}', \quad P^{RI} = \dot{\psi}^{RI} + \dot{\theta} = \sigma \dot{\varepsilon}^e + \theta' \dot{\gamma} + \xi \dot{\gamma}', \quad (11)$$

and, using (5), (10) reduces to $D^{RD} = \sigma^d \dot{\gamma}$ and $D^{RI} = \theta' \dot{\gamma}$, which are non-negative for (6) and (8), respectively. Note that the power spent by the hyperstress ξ makes the free-energy imbalance (10) non-local. Inequalities analogous to (10) were used in Gudmundson (2004); Gurtin and Anand (2005, 2009) to deduce gradient plasticity theories in thermodynamically consistent ways.

The basic difference between the two models is that the plastic energy is stored in the RD model, while it is completely dissipated in the RI model. It follows that plastic strains are partially recoverable in the RD model and totally unrecoverable in the RI models. This constitutive difference reflects on the microstress power-conjugated to $\dot{\gamma}$, which is $\pi^{RD} = \psi'_\gamma + \sigma^d$ and $\pi^{RI} = \theta'$ for the RD and RI model, respectively. While π^{RD} is sum of an energetic and a dissipative viscous term, π^{RI} is totally dissipative.

2.3. Equilibrium

We assume u and γ as independent kinematical descriptors. In addition to (1), we assign the boundary conditions on γ

$$\gamma_t(0) = \gamma_t(l) = 0 \text{ (hard b.c.)}, \text{ or } \gamma'_t(0) = \gamma'_t(l) = 0 \text{ (soft b.c.)}. \quad (12)$$

The equilibrium problem is written in a variational format. Let $E(u, \gamma)$ be the total energy of the body. A configuration (u, γ) is equilibrated if

$$\delta E(u, \gamma; \delta u, \delta \gamma) + \delta W_{NC}(\dot{\gamma}; \delta \gamma) \geq 0, \quad (13)$$

for any admissible perturbation $(\delta u, \delta \gamma)$, with δE the first variation of E , and δW_{NC} the infinitesimal work of the viscous stresses which is present only in the RD model. The total energies of the RD and RI model are

$$E^{RD}(u, \gamma) = \int_0^l \psi^{RD}(u' - \gamma, \gamma, \gamma') dx, \quad E^{RI}(u, \gamma) = \int_0^l (\psi^{RI}(u' - \gamma, \gamma') + \theta(\gamma)) dx. \quad (14)$$

They coincide with the strain energies, since there is no external energy. The infinitesimal viscous work is $\delta W_{NC} = \int_0^l c \dot{\gamma} \delta \gamma dx$ in the RD model, and it does not exist in the RI model. The variational inequality (13) represents a first-order stability condition, and it is typical of constrained equilibrium problems (see Nguyen (2000); Mielke (2005); Del Piero (2013); Pham and Marigo (2013); Alessi et al. (2015)). While RI model is constrained by the dissipation condition (9) the unconstrained RD model, (13) reduces to an equality.

RD model. Since admissible perturbations δu and $\delta \gamma$ can have any sign, the inequality (13) reads

$$\int_0^l (\sigma(\delta u' - \delta \gamma) + \psi'_\gamma \delta \gamma + \xi \delta \gamma' + c \dot{\gamma} \delta \gamma) dx = 0, \quad (15)$$

which is the virtual work equation. The macroscopic and microscopic force balance equations are obtained from (15) by assuming $\delta \gamma = 0$ and $\delta u' = 0$ (i.e. $\delta \gamma = -\delta \varepsilon^e$), respectively. They are

$$\sigma' = 0, \quad \sigma - \psi'_\gamma + \xi' - c \dot{\gamma} = 0. \quad (16)$$

Remark. Initial elastic regime. Let us assume that $\psi'_\gamma(0) > 0$. At the initial instant $t = 0$, γ and the dissipated force $c \dot{\gamma}$ are null. Thus, equation (16)₂ is satisfied by the elastic deformation $\varepsilon_0^e = \psi'_\gamma(0)/E$, which represents an initial elastic deformation state corresponding to the stress $\sigma_0 = \psi'_\gamma(0)$. The elastoplastic deformation evolves from such an initial elastic state, according to the evolution equation

$$E(\varepsilon^e - \varepsilon_0^e) - (\psi'_\gamma - \psi'_\gamma(0)) + A \gamma'' - c \dot{\gamma} = 0. \quad (17)$$

We conclude that the constitutive assumption $\psi'_\gamma(0) > 0$ characterizes materials which exhibit an initial purely elastic behavior.

RI model. From (9), γ can only grow, and thus an admissible perturbation is such that $\delta\gamma \geq 0$. The variational inequality (13) is rewritten as

$$\int_0^l (\sigma(\delta u' - \delta\gamma) + \xi\delta\gamma' + \theta'\delta\gamma) dx \geq 0. \quad (18)$$

For perturbations with $\delta\gamma = 0$, we deduce the macroscopic stress balance (16)₁, while for arbitrary perturbations such that $\delta\varepsilon^e + \delta\gamma = 0$, we get the inequality

$$\sigma \leq \theta' - \xi', \quad (19)$$

which represents a yield condition, which states that the stress σ cannot be greater than the yield limit $\theta' - \xi'$, and represents the yield condition of classical plasticity.

2.4. Incremental evolution problem

Let (u_t, γ_t) be the solution at the instant t , which is supposed to be known. For a given time step τ , the solution at the instant $t + \tau$ is approximated by the first-order Taylor expansion

$$u_{t+\tau} = u_t + \tau\dot{u}_t, \quad \gamma_{t+\tau} = \gamma_t + \tau\dot{\gamma}_t, \quad (20)$$

and the strain energies (14) are approximated by the second-order development

$$E_{t+\tau}(\dot{u}_t, \dot{\gamma}_t) = E_t + \tau\dot{E}_t(\dot{u}_t, \dot{\gamma}_t) + \frac{1}{2}\tau^2\ddot{E}_t(\dot{u}_t, \dot{\gamma}_t). \quad (21)$$

The unknown pair $(\dot{u}_t, \dot{\gamma}_t)$ satisfies the variational inequality

$$\delta E_{t+\tau}(\dot{u}_t, \dot{\gamma}_t; \delta\dot{u}, \delta\dot{\gamma}) + \delta W_{NC}(\dot{\gamma}_t; \delta\dot{\gamma}) \geq 0, \quad (22)$$

for any admissible perturbations pair $(\delta\dot{u}, \delta\dot{\gamma})$, which represents the linear approximation of (13) with respect to the known configuration (u_t, γ_t) .

RD model. By assuming $\delta\dot{\gamma} = 0$ and $\delta\dot{u}' = 0$ in (22), we obtain the macroscopic and microscopic evolution equations

$$(\dot{u}'_t - \dot{\gamma}_t)' = 0, \quad E(\dot{u}'_t - \dot{\gamma}_t) - \left(\psi''_{\gamma}(\gamma_t) + \frac{c}{\tau} \right) \dot{\gamma}_t + A\dot{\gamma}_t'' = -\frac{\sigma_t^d}{\tau}, \quad (23)$$

with the boundary conditions

$$\begin{aligned} \dot{u}_t(0) = 0, \quad \dot{u}_t(l) = l\dot{\varepsilon}_t, \\ \dot{\gamma}_t(0) = \dot{\gamma}_t(l) = 0 \text{ (hard b.c.)}, \quad \text{or} \quad \dot{\gamma}_t'(0) = \dot{\gamma}_t'(l) = 0 \text{ (soft b.c.)}. \end{aligned} \quad (24)$$

Equations (23) can be directly obtained from (16) by linearization.

RI model. Assuming $\delta\dot{\gamma} = 0$ in (22), leads to macroscopic evolution equation (23)₁, and setting $\delta\dot{u} = 0$, gives

$$\delta E_{t+\tau}^{RI}(\dot{u}_t, \dot{\gamma}_t, 0, \delta\dot{\gamma}) = \int_0^l (f_t + \tau\dot{f}_t) \delta\dot{\gamma} dx + [(\xi_t + \tau\dot{\xi}_t)\delta\dot{\gamma}]_0^l \geq 0, \quad \text{with } f_t = \theta'_t - \sigma_t - \xi'_t. \quad (25)$$

In (25), the boundary terms are null if hard or soft boundary conditions are assigned. Since $\dot{\gamma}_t + \delta\dot{\gamma}$ must be non-negative for the dissipation inequality (9), the remaining integral term is non-negative: (i) if $\dot{\gamma}_t = 0$, then $\delta\dot{\gamma} \geq 0$, and (25) is satisfied if $f_t + \tau\dot{f}_t \geq 0$; (ii) if $\dot{\gamma}_t > 0$, $\delta\dot{\gamma}$ can have any sign, and (25) is satisfied if $f_t + \tau\dot{f}_t = 0$. Summing up these two situations, we obtain the Kuhn-Tucker conditions

$$\dot{\gamma}_t \geq 0, \quad f_t + \tau\dot{f}_t \geq 0, \quad (f_t + \tau\dot{f}_t)\dot{\gamma}_t = 0, \quad (26)$$

equivalent to (25), which state that the force is equal to the yield force when γ evolves, and represents the flow rule of plasticity. Equations (23)₁, (26) and (24) are necessary conditions for a minimum of the total energy $E_{t+\tau}$, i.e., for $(\dot{u}_t, \dot{\gamma}_t)$ to be solution of the following constrained quadratic programming problem

$$(\dot{u}_t, \dot{\gamma}_t) = \operatorname{argmin}\{E_t(\dot{u}_t, \dot{\gamma}_t), \dot{\gamma}_t \geq 0; \dot{u}_t(0) = 0, \dot{u}_t(l) = l\dot{\varepsilon}_t, \\ \dot{\gamma}_t(0) = \dot{\gamma}_t(l) = 0 \text{ (hard b.c.)}, \text{ or free } \dot{\gamma}_t(0) = \dot{\gamma}_t(l) \text{ and } \dot{\xi}_t(0) \text{ (soft b.c.)}\}. \quad (27)$$

In the numerical code we prefer to solve the problem (27), instead of the equivalent relations (26), since very efficient subroutines for quadratic programming are freely available in many computing languages.

Remark. Initial elastic regime. Initial elastic deformation regimes are found if $\theta'(0) > 0$, as in the RD model (see the remark in Sect. 2.3). Indeed, at the initial instant $t = 0$, $f_0 = \theta'(0) > 0$, since $\sigma_0 = \xi_0 = 0$, and, from (26), $\dot{\gamma}_0 = 0$. Thus only elastic deformation occurs, until the stress σ equals $\theta'(0)$. At this point, inelastic deformation can take place since $f_t = 0$.

3. Analytical solutions

Analytical solutions can be determined only in some special cases. One of these is the case of evolution from homogeneous configurations. Let us assume that at the instant t , γ_t is homogenous. The stress is $\sigma_t = \psi'_\gamma(\gamma_t)$ for the RD model, and $\sigma_t = \theta'_t$ for the RI model, according to (16)₂ and (19) respectively ($\xi'_t = A\gamma''_t = 0$ since γ_t is constant).

RD model. Under these assumptions, the evolution equations (23) for the RD model reduces to equations with constant coefficients, which can be easily solved. Since, from (23)₁, $(\dot{u}'_t - \dot{\gamma}_t)$ is constant in $(0, l)$, \dot{u}'_t can be written in terms of $\dot{\gamma}_t$ as follows: $\dot{u}'_t = \dot{\gamma}_t + \dot{\varepsilon}_t - \frac{1}{l} \int_0^l \dot{\gamma}_t dx$. Substituting this expression in (23)₂, we obtain an integro-differential equation for $\dot{\gamma}$. To make explicit the dependence on the deformation rate $\dot{\varepsilon}$, we write $\tau = \delta\varepsilon/\dot{\varepsilon}$ in (23)₂, with $\delta\varepsilon$ the deformation increment imposed in the step τ . If we assume hard boundary conditions, the solution of (23)₂ is

$$\begin{aligned} \dot{\gamma} &= \frac{\dot{\varepsilon}(E + \sigma^d/\delta\varepsilon)}{\psi''_\gamma + E\varphi_1(kl) + c\dot{\varepsilon}/\delta\varepsilon} \left(1 - \frac{\cosh k(l/2 - x)}{\cosh kl/2} \right), & \text{if } \psi''_\gamma > -\frac{c\dot{\varepsilon}}{\delta\varepsilon}, \\ \dot{\gamma} &= \frac{6\dot{\varepsilon}(E + \sigma^d/\delta\varepsilon)}{12A + E l^2} x(l - x), & \text{if } \psi''_\gamma = -\frac{c\dot{\varepsilon}}{\delta\varepsilon}, \\ \dot{\gamma} &= \frac{\dot{\varepsilon}(E + \sigma^d/\delta\varepsilon)}{\psi''_\gamma + E\varphi_2(kl) + c\dot{\varepsilon}/\delta\varepsilon} \left(1 - \frac{\cos k(l/2 - x)}{\cos kl/2} \right), & \text{if } \psi''_\gamma < -\frac{c\dot{\varepsilon}}{\delta\varepsilon}, \end{aligned} \quad (28)$$

with

$$k = \sqrt{\frac{1}{A} \left| \psi''_{\gamma} + \frac{c\dot{\varepsilon}}{\delta\varepsilon} \right|}, \quad \varphi_1(kl) = 1 - \frac{2}{kl} \tanh \frac{kl}{2}, \quad \varphi_2(kl) = 1 - \frac{2}{kl} \tan \frac{kl}{2}. \quad (29)$$

In the case of soft boundary conditions, the solution is homogeneous

$$\dot{\gamma} = \frac{\dot{\varepsilon}(E + \sigma^d/\delta\varepsilon)}{\psi''_{\gamma} + E + c\dot{\varepsilon}/\delta\varepsilon}. \quad (30)$$

The index t is omitted for the sake of conciseness. Schematic representations of the solution as function of ψ''_{γ} are depicted in Fig. 2(a).

In the case of hard boundary conditions, the solution extends in the whole domain if $\psi''_{\gamma} \geq -4\pi^2 A/l^2 - c\dot{\varepsilon}/\delta\varepsilon$ (*full-size* solution), and it localizes if $\psi''_{\gamma} < -4\pi^2 A/l^2 - c\dot{\varepsilon}/\delta\varepsilon$ (*localized* solution). In the full-size regime, we distinguish the hyperbolic solution (28)₁ and trigonometric solution (28)₃. In the localized case, γ grows in a central zone of length $2\pi/k$, and it reduces outside of it (plastic unloading). We notice that the separation value $\psi''_{\gamma} = -4\pi^2 A/l^2 - c\dot{\varepsilon}/\delta\varepsilon$ between the regions of full-size and localized solutions decreases as $\dot{\varepsilon}$ increases, suggesting that localization is facilitated when a small $\dot{\varepsilon}$ is assigned. The numerical simulations of Sect. 4.1 have shown results in agreement with this. Indeed it was found that the strain localization process and the consequent plastic slip patterning are delayed, and, eventually, avoided when large values of $\dot{\varepsilon}$ are assumed.

In the case of soft boundary conditions, $\dot{\gamma}$ is always homogeneous. However, it was proved in Yalcinkaya et al. (2011) that the homogenous solution is unstable when $\psi''_{\gamma} < 0$. The numerical simulations have confirmed this result, and, furthermore, they have exhibited a correlation of direct proportionality between $\dot{\varepsilon}$ and the instant at which the deformation starts to localize within the evolution process. Further investigations on this stability issue are left to future work.

RI model. When we assume γ_t homogenous and $\sigma_t = \theta'_t$ in the RI model, the Kuhn-Tucker problem (26) simplifies as follows

$$A\dot{\gamma}_t'' - \theta_t'' \dot{\gamma}_t = -\dot{\sigma}_t, \quad \text{if } \dot{\gamma}_t > 0; \quad \dot{\sigma}_t \leq \theta_t'' \dot{\gamma}_t - A\dot{\gamma}_t'', \quad \text{if } \dot{\gamma}_t = 0. \quad (31)$$

Equation (23)₂ of the RD model and equation (31)₁ of the RI model exhibit striking similarities. Indeed (23)₂ differs from (31)₁ only for terms multiplied by $1/\tau$, which disappears when $\dot{\varepsilon} = 0$, since $1/\tau = \dot{\varepsilon}/\delta\varepsilon$. The problem (31) was solved for hard boundary conditions in Del Piero et al. (2013) and soft boundary conditions in Lancioni (2015). The solutions, which depend on the value of θ'' , are schematically represented in Fig. 2(b), and we refer to the above mentioned papers for the explicit results. When hard boundary conditions are applied, $\dot{\gamma}$ is uniform if $\theta'' > -4\pi^2 A/l^2$, and it localizes in subregions of $(0, l)$ of length $2\pi\sqrt{A/\theta''}$, vanishing outside of them, if $\theta'' < -4\pi^2 A/l^2$. When soft boundary conditions are assigned, $\dot{\gamma}$ is homogeneous if $\theta'' > -2\pi^2 A/l^2$, and it localizes at the boundaries, in zones of length $\pi\sqrt{A/\theta''}$, if $\theta'' < -2\pi^2 A/l^2$.

The analytical solutions of both models present many similarities, but some differences as well. We highlight two differences related to the two main distinguishing features of the models here: the dependence on the deformation rate of the RD model and the totally dissipative nature of the plastic energy in the RI model. The first concerns the fact that transition from full-size solutions

to localized solutions depends on $\dot{\varepsilon}$ in the RD model, while it is independent of rate in the RI model. The second concerns the localized solution, which accounts for plastic recovery outside the localization zone only in the RD model. The plastic deformation never decreases in the RI model, being always totally dissipated.

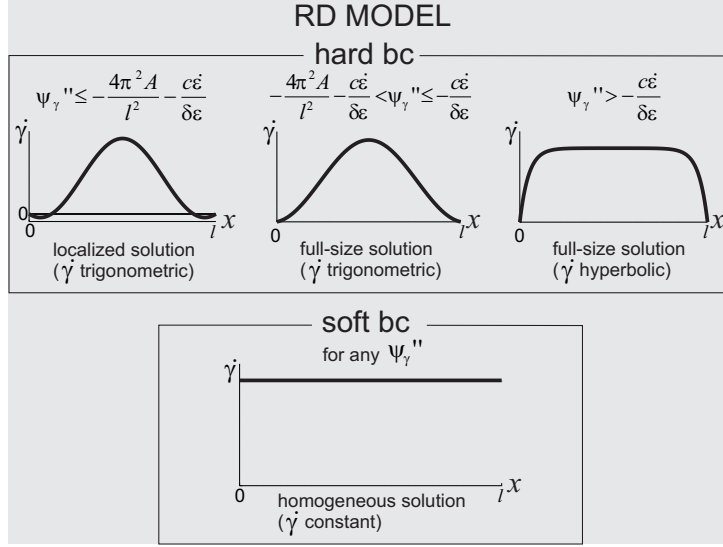
4. Numerical results

The incremental problems (23), (24) for the RD model, and (27) for the RI model are solved numerically, following a finite element procedure. The domain is subdivided into finite elements and, within each element, the displacement and plastic deformation rates are approximated by using quadratic and linear shape functions, respectively. At each time increment, the solution of the linearized problem (23) in the RD model is refined through a Newton-Raphson scheme, while the solution of the approximated minimum problem (27) in the RI model is improved by means of a Sequential Quadratic Programming algorithm. In the latter, each quadratic programming problem is solved through the projection method (see e.g. Gill et al. (1981)). Both implementation procedures are quite straightforward, and no particular convergence problems have been encountered. It is observed that viscosity in the RD model plays a regularizing role as well in addition to the non-local term. More attention must be focused on the RI model implementation: sufficiently small time steps must be considered to avoid convergence loss, when the evolution undergoes sharp deformation changes.

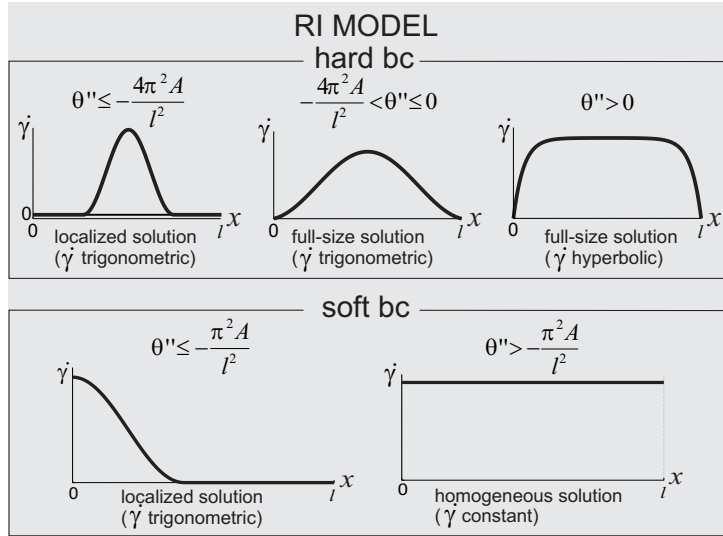
4.1. Numerical modeling of plastic slip patterning

As explained in Section 2, the first numerical example addresses the formation of microstructures in metallic materials. In this simplified 1D setting, it corresponds to the analysis of the evolution of heterogeneous plastic shear deformation in a semi-infinite layer with thickness l , as shown in Fig. 1(a). The patterning of plastic slip is investigated when soft and hard boundary conditions (24) are assigned in both rate-dependent and rate-independent frameworks. According to the usual notation for shear problems, we define the macroscopic shear strain Γ and the shear stress T , which correspond to ε and σ , respectively, of the previous theoretical sections.

The layer is made of steel and its thickness is $l = 1$ mm. Since the shear problem is considered, Young's modulus E used in the above theoretical sections is replaced by the shear modulus $G = 78.9$ GPa, which corresponds to the Young's modulus $E = 210$ GPa and the Poisson's ratio $\nu = 0.33$. As in Yalcinkaya et al. (2011), we set $c = s/\dot{\gamma}_0 = 7$ MPa/s. The length scale enters the formulation via $A = ER^2/(16(1 - \nu^2))$ as, e.g., used in Bayley et al. (2006), where R physically represents the radius of the dislocation domain contributing to the internal stress field. In this example $R = 0.1$ mm, corresponding to $A = 147.29$ N. For the plastic energy density (ψ_γ in the RD model and θ in the RI model) a Landau-Devonshire type of potential is assumed, which is asymmetric, where the second well is shifted up with respect to the first (Yalcinkaya et al. (2011)), $\psi_\gamma = \theta = 1.525 \times 10^8 \gamma^4 - 5.2 \times 10^6 \gamma^3 + 5.25 \times 10^4 \gamma^2$ MPa. Graphs of the plastic energy density, and its first derivative are represented in Fig. 3. The binodal and spinodal points are $\gamma_{b1} = 0.0018$, $\gamma_{b2} = 0.0153$, $\gamma_{s1} = 0.0046$, and $\gamma_{s2} = 0.0124$ respectively. The stress corresponding to the Maxwell line is $T_M = 139.3281$ MPa. which is basically $\psi_\gamma(\gamma_{b2}) - \psi_\gamma(\gamma_{b1}) = T_M(\gamma_{b2} - \gamma_{b1})$.



(a)



(b)

Figure 2: Scheme of the analytical solutions in the case of RD (a) and RI (b) model. In the RD model, three different types of solution are found when the hard bc's are assigned, depending on the value of $\Psi_\gamma''(\gamma_i)$ (first box in Fig. (a)). For the soft bc's, the solution is always homogeneous (second box in Fig. (a)). In the RI model, the solution depends on the value of $\theta''(\gamma_i)$: three different regimes are distinguished when the hard bc's are assigned (first box in Fig. (b)), and two regimes (homogeneous and localized) characterize the solution in the case of soft bc's (second box in Fig. (b)).

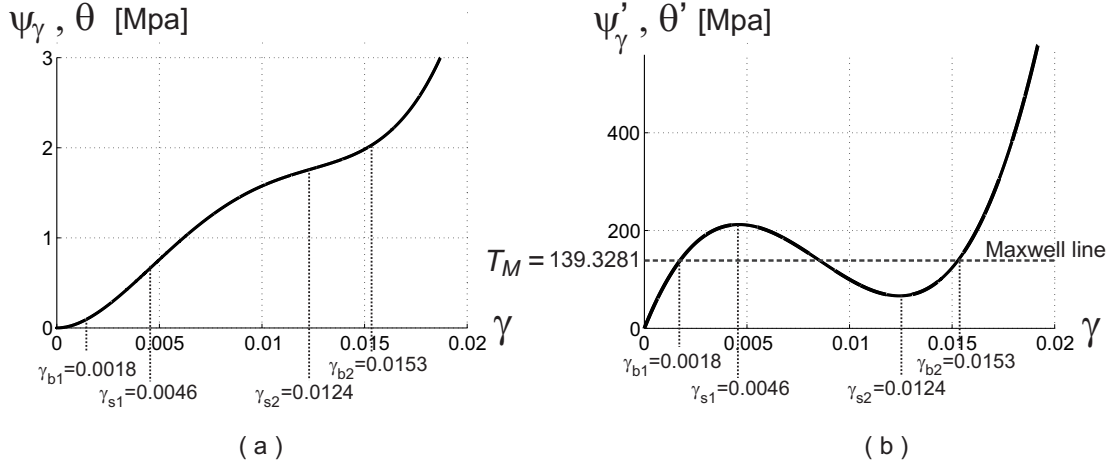


Figure 3: Double-well plastic energy density (a), and its derivative (b).

The stress vs. strain curves obtained from the RI (solid line) and RD (dashed line) model are represented in Fig. 4 for the case of soft and hard boundary conditions. For the RD model, the deformation rates $\dot{\Gamma} = 0.001, 0.02, 0.1, 1, 10 \text{ s}^{-1}$ are considered. The response curves of the RD model get closer to the curve for the RI model, as the deformation rate decreases.

Considering the deformation evolution, first we analyze the case of soft boundary conditions. In Fig. 5, the evolution of the plastic slip field γ is plotted at different values of the imposed shear strain Γ , for the RI model and for the RD model at low shear rate ($\dot{\Gamma} = 0.001 \text{ s}^{-1}$).

In the case of the RD model, for high deformation rates ($\dot{\Gamma} = 1, 10 \text{ s}^{-1}$), the plastic strain is always homogeneous. For sufficiently low rates ($\dot{\Gamma} = 0.001, 0.02, 0.1 \text{ s}^{-1}$), three main regimes are distinguished on the stress vs. strain response: small homogeneous deformation (hardening branch), plastic slip wave evolution (stress-plateau), large homogeneous deformation (hardening branch). The deformation starts to localize during the sharp softening of the stress vs. strain response curve. As the deformation rate decreases, the stress drop occurs earlier and the length of the softening branch increases. As discussed in Sect. 3, the homogeneous solution always solves the evolution problem, but for concave plastic potentials, it is unstable, and, thus, any small disturbance leads to a stable localization evolution. In these simulations the disturbances inherent in the numerical calculus are sufficient to induce localization. The sharp softening branch is followed by a stress-plateau which corresponds to the movement of the localization band from the right side to the left side of the domain. Decreasing the deformation rate, the plateau of the response curve lowers, and it approaches to the Maxwell line. The final transition to homogenous deformation is accompanied by a stress drop in the stress vs. strain curve, which shifts to the right as the deformation rate is increased. **We notice that stress-strain curves are always continuous. The softening branches are only apparently discontinuous drops, but actually they are smooth quickly decreasing curves.**

The behavior predicted by the RI model is analogous to that of the RD model for small $\dot{\Gamma}$: the deformation initially evolves homogeneously, then it localizes on the right side and propagates

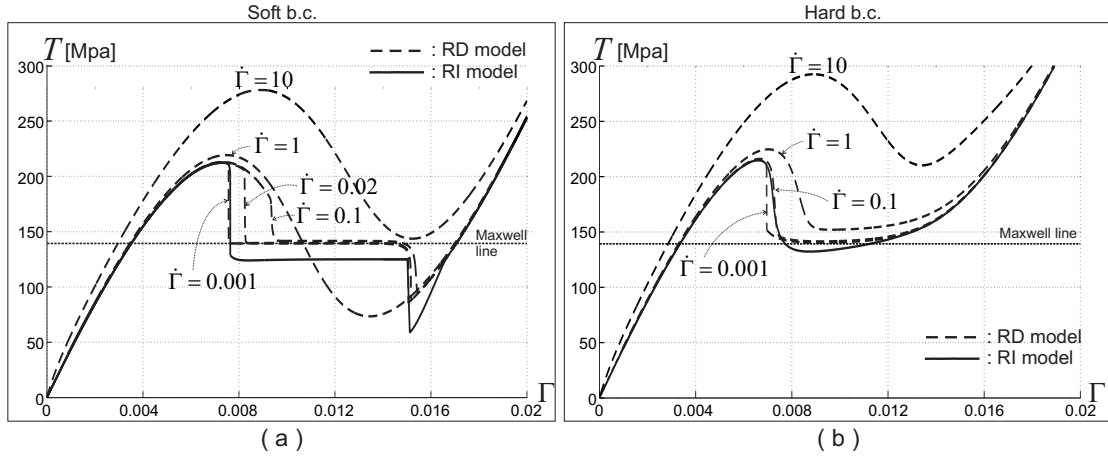


Figure 4: Response curves in the cases of (a) soft and (b) hard boundary conditions with $\dot{\Gamma} = [s^{-1}]$.

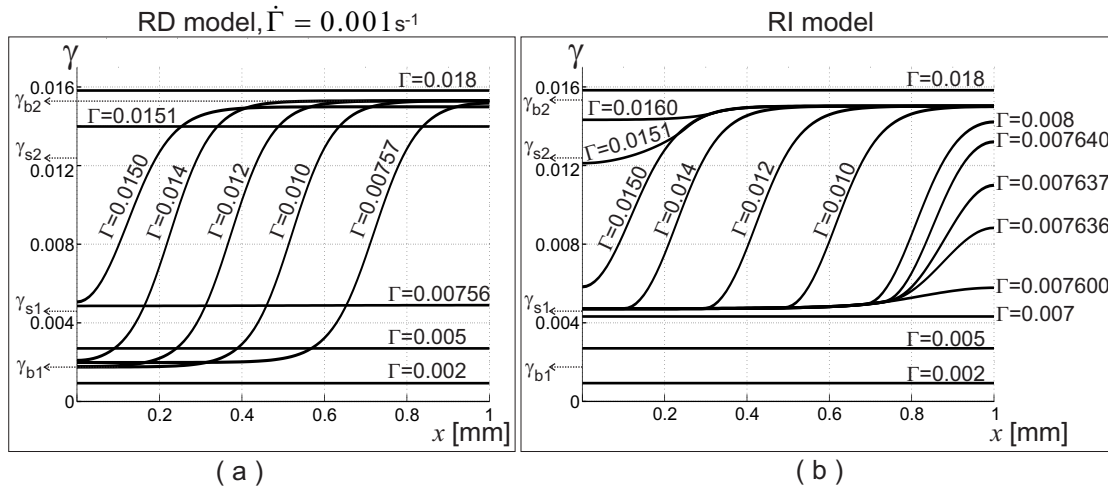


Figure 5: Profiles of γ at different values of Γ with soft boundary conditions: (a) RD model with $\dot{\Gamma} = 0.001 s^{-1}$, (b) RI model.

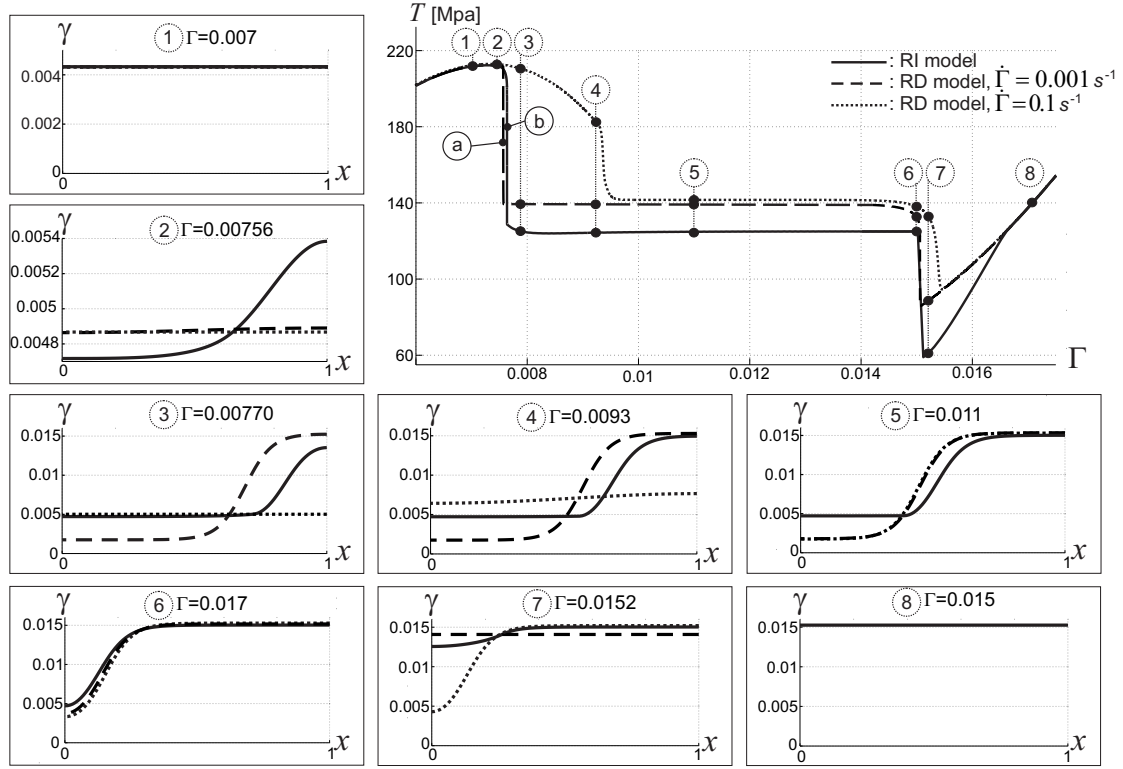


Figure 6: Comparison of γ estimated at eight different states with soft boundary conditions. RI model: solid line; RD model with $\dot{\Gamma} = 0.001 \text{ s}^{-1}$: dashed line; RD model with $\dot{\Gamma} = 0.1 \text{ s}^{-1}$: dotted line.

towards to the left, and, finally, it increases homogenously. According to the analytical results of Sect. 3, localization starts when γ reaches the value $\theta''^{-1}(-\pi^2 A/l)$, which is very close to the spinodal value γ_{s1} .

Focusing on the softening phase, which corresponds to the microstructure formation, we observe that in the RD model, the localization front moving from right to left is 0.25 mm wide. Plastic strain has saturated at a value of $\gamma = \gamma_{b2} = 0.0153$ to the right of the front, while at the left it rapidly reduces to a constant value $\gamma = \gamma_{b1} = 0.0018$. The front for the RI model has a similar width, but the strain downstream of the front remains constant at $\gamma \simeq \gamma_{s1} = 0.0046$, the value at which localization is initiated. In the RI model, the plastic energy is totally dissipated, and thus γ can only grow. On the other hand, the energy ψ_γ of the RD model is stored, and therefore γ can be partially recovered, which explains the reduction of γ outside the localization zone. Plastic energy recovery is also evident at the end of the slip patterning evolution, when the deformation becomes homogeneous. Increasing Γ from 0.0150 to 0.0151, results in a significant reduction in γ over the entire domain.

In Fig. 6 a thorough comparison of the plastic deformation predicted by the RI model and the RD model (with $\dot{\Gamma} = 0.001 \text{ s}^{-1}$ and 0.1 s^{-1}) is presented. Deformation profiles corresponding to eight different states, indicated by dots on the stress vs. strain response curve, are analyzed. In the initial hardening regime, the two models give same solutions (state 1), while differences

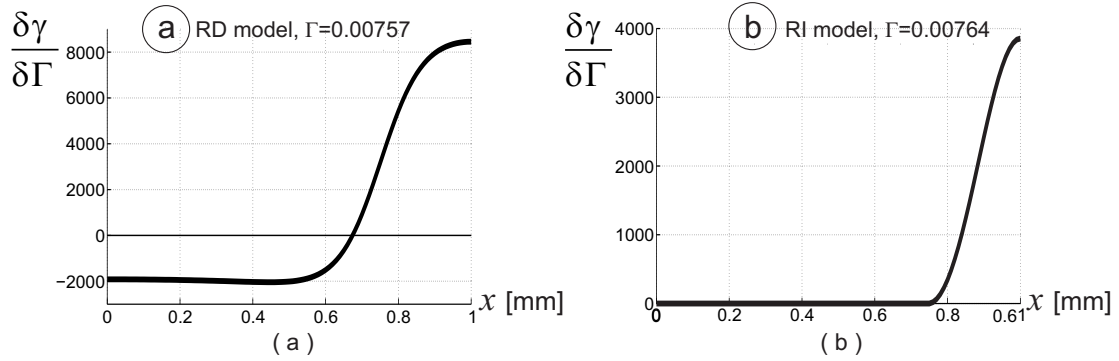


Figure 7: Ratio $\delta\gamma/\delta\Gamma$ at the onset of the localization with soft boundary conditions: (a) RI model, and (b) RD model with $\dot{\Gamma} = 0.001 \text{ s}^{-1}$.

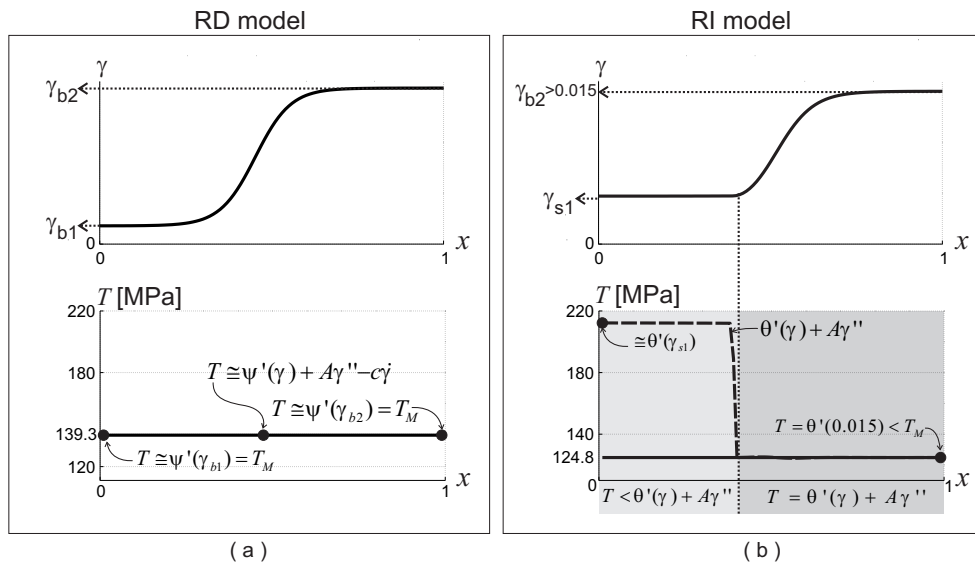


Figure 8: Shear strain and stress $\Gamma = 0.011$ with soft boundary conditions at (state 5 of Fig. 6) given by the RD model with $\dot{\Gamma} = 0.001 \text{ s}^{-1}$ (a) and the RI model (b).

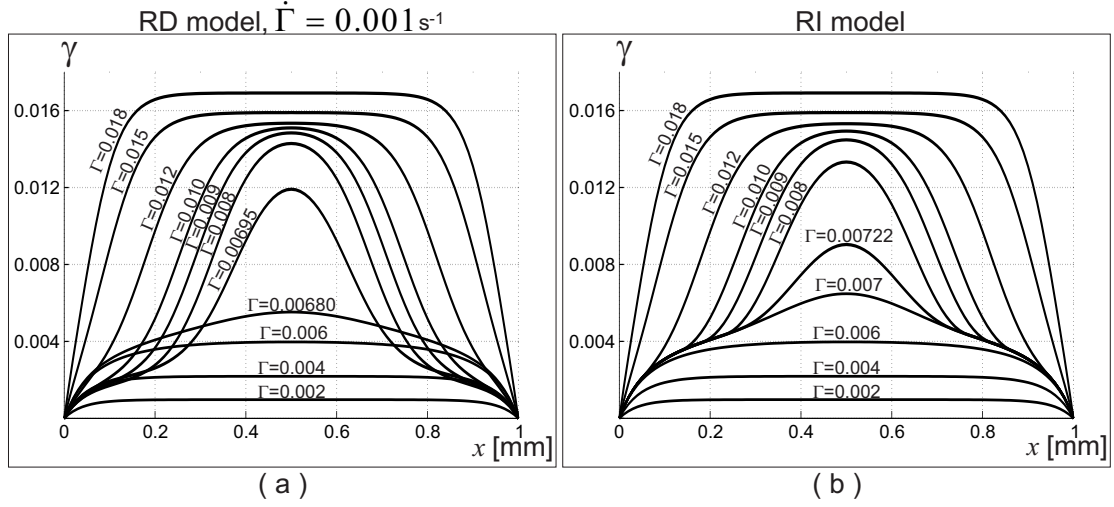


Figure 9: Profiles of γ at different values of Γ with hard boundary conditions: (a) RD model with $\dot{\Gamma} = 0.001 \text{ s}^{-1}$, (b) RI model.

arise in the consecutive softening phase, as pointed out above. Two further distinguishing features deserve comment. First, the transition from homogenous to localized deformation is much sharper in the RD model than in the RI model (states 2 and 3). This difference is confirmed by the graphs of the ratio $\delta\gamma/\delta\Gamma$ at the deformation states A and B of the sharp softening branches (see Fig. 6), plotted in Fig. 7. Indeed, the values attained in the localization zone by the RD model are twice those of the RI model, although high values are obtained in both cases. In the RD model, large negative velocities are reached outside the localization zone, where the plastic deformation is recovered. The second remark concerns the delay of localization when the rate $\dot{\Gamma} = 0.1 \text{ s}^{-1}$ is considered (states 3 and 4). In this case, a long softening branch of moderate slope forms in the stress vs. strain curve, before the sharp softening phase, in which the deformation only slightly deviates from the homogeneous configuration (states 3 and 4). If we pass to the next stress-plateau phase, corresponding to the plastic wave propagation, the solutions predicted by the RD model are coincident (state 5). In the low and high plastic slip zones, placed on the left and right sides of the domain, γ attains the values γ_{b1} and γ_{b2} , respectively, of the binodal points. Since in these zones γ is practically homogeneous and stationary, from (16)₂, the corresponding shear stress is $T = \psi'_\gamma(\gamma_{b1}) = \psi'_\gamma(\gamma_{b2}) = T_M$, which remains throughout the whole slip patterning process. A schematic sketch of the strain and stress distribution is shown in Fig. 8(a). The corresponding distribution for the RI model is shown in Fig. 8(b). In the high slip zone, on the right side, γ assumes values smaller than γ_{b2} , and, thus, $T < T_M$. We note that (19) is satisfied as equality in the zone crossed by the wave of high plastic deformation and as inequality outside of the zone. Finally, going back to Fig. 6, further discrepancies are evident at the end of the slip patterning (state 7). They are due to the above discussed phenomena of strain recovery, allowed in the RD model and forbidden in the RI model, with delays in the recovery process evident at high $\dot{\Gamma}$.

In the case of hard boundary conditions, the stress vs. strain responses are presented in Fig.

4(b). Similar to the previous soft boundary case, as the deformation rate decreases, the results of the RD model approach to the prediction of the RI model. Three different regimes are distinguished: (i) an initial hardening phase in which deformation is homogeneous, except in the boundary layer development at each end, (ii) a softening branch in which the deformation localizes in the middle of the domain, (iii) a stress-plateau characterized by the evolution of the plastic slip toward the boundaries, and (iv) a final smooth hardening branch, where the deformation field evolves in a similar way to the initial hardening phase. The corresponding evolution of the plastic slip field is presented in Fig. 9 for the RI and RD models with $\dot{\Gamma} = 0.001 \text{ s}^{-1}$. Although not shown here, the RD model also produces an homogeneous deformation with a boundary layer at high deformation rates.

The results show a good agreement between the two models at low deformation rates, while at high deformation rates the RD model produces an homogeneous deformation field. In the next section localization leading to necking of a homogeneous bar is studied.

5. Numerical modeling of necking and fracture in tensile steel bars

We consider an homogeneous steel bar (Young's modulus $E = 210 \text{ GPa}$) of length $l = 140 \text{ mm}$, as shown in Fig. 1(c), clamped at the left and subjected to the tensile displacement εl at the right. Since we are dealing with a uniaxial tensile problem, we denote the longitudinal plastic deformation as ε^p , in place of γ , which usually denotes the shear strain.

We assume the plastic energy and the non-local coefficient A proposed in Lancioni (2015), which have been determined from a phenomenological fit to experimental results on smooth and notched bone-shaped samples. In this problem we interpret σ and ε as nominal quantities, thus the phenomenological fits employed here include the effects of geometric as well as material softening.

The plastic energy is the piecewise cubic function represented in Fig. 10. It is a convex function in the interval $0 \leq \varepsilon^p < 0.16$, a concave function for $0.16 \leq \varepsilon^p < 0.7$, and a constant function for $\varepsilon^p > 0.7$. The analytical expression of ψ_{ε^p} or, equivalently, θ is

$$\psi_{\varepsilon^p} = \begin{cases} 0.37\varepsilon^p + 0.78\varepsilon^{p2} - 1.59\varepsilon^{p3}, & 0 \leq \varepsilon^p < 0.16, \\ 0.07 + 0.5(\varepsilon^p - 0.16) - 2.46 \cdot 10^{-4}(\varepsilon^p - 0.16)^2 - 0.57(\varepsilon^p - 0.16)^3, & 0.16 \leq \varepsilon^p < 0.7, \\ 0.25 & \varepsilon^p \geq 0.7. \end{cases} \quad (32)$$

For $\varepsilon^p > 0.7$, the bar deforms plastically without any increase in plastic energy, and this corresponds to complete fracture. Thus, the simulations presented in the following are interrupted when ε^p reaches the fracture value of $\varepsilon_2^p = 0.7$. For the non-local coefficient and the friction coefficient, we assume $A = 2 \text{ kN}$, and $c = 0.015 \text{ GPa/s}$, respectively.

Note that A includes a hidden phenomenological length scale parameter, however it could be related to the diameter of the bar, which is the dominant length scale in this problem. The viscous coefficient c has also been determined by a curve fitting procedure.

In Fig. 11, experimental and numerical $\sigma - \Delta s$ curves are compared. The experimental test has been performed at ‘‘Laboratory of Materials and Structures Testing’’ of Polytechnic University of Marche (Ancona, Italy), by using a Universal Testing Machine, with deformation rate $\dot{\varepsilon} = 0.8 \cdot 10^{-3} \text{ s}^{-1}$. In the x -axis, Δs represents the relative displacement between two points, indicated by dots in Fig. 1(b), which define an initial gauge length of 80 mm and σ represents the nominal stress.

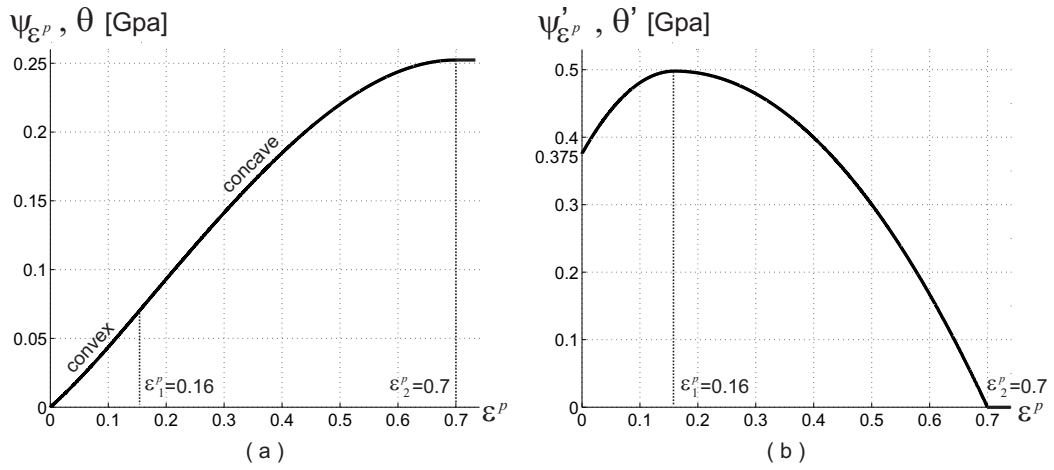


Figure 10: Convex-concave plastic energy density (a), and its first (b).

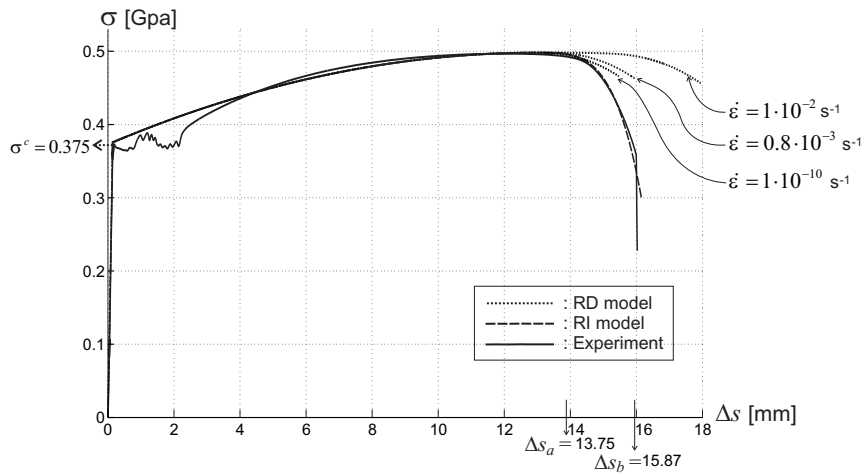


Figure 11: $\sigma - \Delta l$ response curves given by the experiment (solid line), the RI model (dashed line), and the RD model (dotted line).

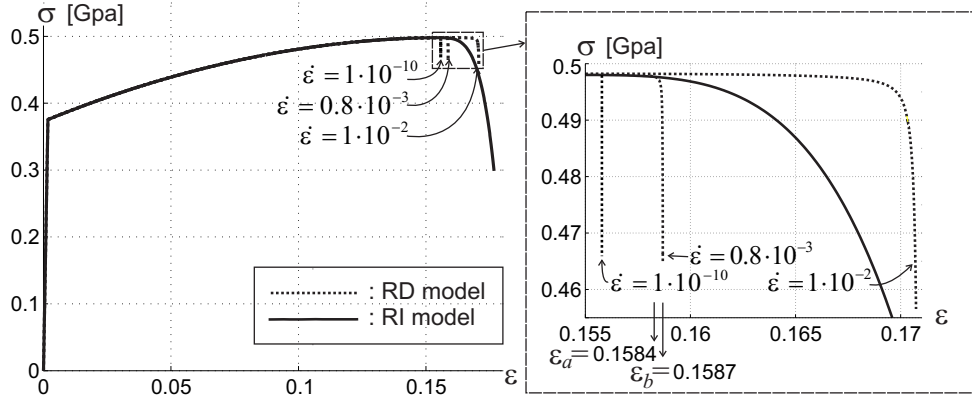


Figure 12: $\sigma - \varepsilon$ response curves. Only low deformation rates are considered. $\dot{\varepsilon} = [\text{s}^{-1}]$.

For the RD model, three different deformation rates $\dot{\varepsilon} = 1 \cdot 10^{-10}$, $0.8 \cdot 10^{-3}$, and $1 \cdot 10^{-2}$ s^{-1} are considered, which are sufficiently low to get softening and localization. The simulations predict three phases: an initial elastic phase, which is interrupted when σ reaches the yield value $\sigma^c = 0.375$ GPa, an hardening phase, and a final softening phase. The RI and RD models give practically the same hardening branches, however they differ in predicting the softening part. The softening response of the RI model is long and sloped, which is quite close to the experimental curve, while the response of the RD model is shorter, and it strongly depends on the deformation rate $\dot{\varepsilon}$. In Fig. 12, the stress vs. strain response is plotted within the softening regime for the same deformation rates and parameters. A steeper slope of the softening branch of the RD model is observed in comparison to Fig. 11, which is due to different deformation measures considered in the horizontal axes, as explained in the following paragraph. The curves for the RD model are significantly different than that for the RI model. For this problem even at very low deformation rates RD model does not asymptote to the RI model at low strain rates. Notice that the solution predicted by the RD model with $\dot{\varepsilon} = 1 \cdot 10^{-10}$ s^{-1} evolves through a series of steady states, since $\dot{\varepsilon}$ is so small that the process is insensitive to viscosity.

The evolution of ε^p is described in Fig. 13, where the results of the RI model and RD model with $\dot{\varepsilon} = 0.8 \cdot 10^{-3}$ s^{-1} are compared. In both cases, the softening phase is characterized by a progressive localization of ε^p in smaller and smaller portions in the middle of the bar, up to final fracture, which occurs when ε^p reaches the critical value $\varepsilon_2^p = 0.7$. Thus both the RI and RD models describe fracture as the termination of a strain localization process. **But the description differ outside the localization zone: for the RI model, ε^p remains constant, and only the elastic deformation ε^e reduces, since $\delta\varepsilon^e = \delta\sigma/E < 0$ (perfect elastic unloading); for the RD model, ε^p reduces outside the localization zone, being partially recovered (elasto-plastic unloading). In the latter case, the strain increase in the localization zone is slightly larger than the strain reduction outside. This explains the steeper slope of the softening branches of Fig. 12.** In Fig. 13(c), u' is plotted for two different states at $\varepsilon_a = 0.1584$ and $\varepsilon_b = 0.1587$, corresponding to the beginning and the end of the softening phase (see the enlarged zone in Fig. 12). Since $\varepsilon = l^{-1} \int_0^l u' dx$, the increase of deformation at softening is $\varepsilon_b - \varepsilon_a = l^{-1}(A_1 - 2A_2 - 2A_3) = 0.0003$, with A_1 ,

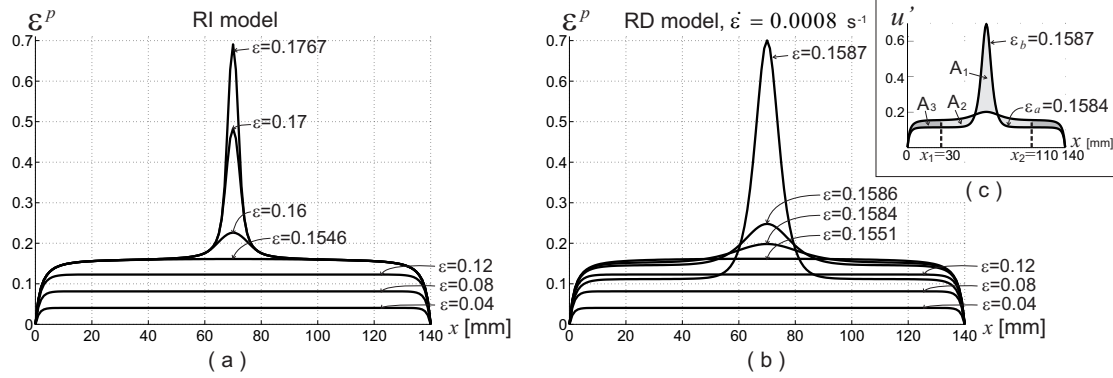


Figure 13: Profiles of ε^p at different values of ε : (a) RI model, (b) RD model with $\dot{\varepsilon} = 0.0008 \text{ s}^{-1}$. (c) u' at the beginning and ending of the softening phase.

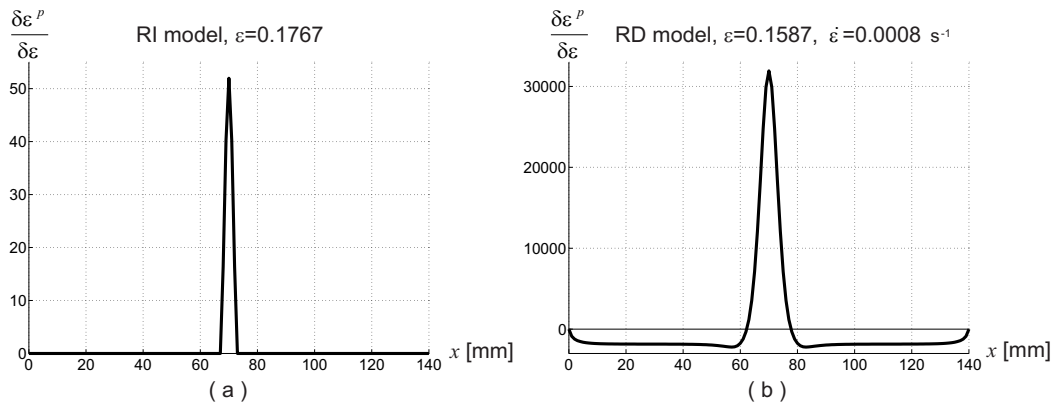


Figure 14: Incremental ratio $\delta \varepsilon^p / \delta \varepsilon$ at fracture: (a) RI model, and (b) RD model with $\dot{\varepsilon} = 0.0008 \text{ s}^{-1}$.

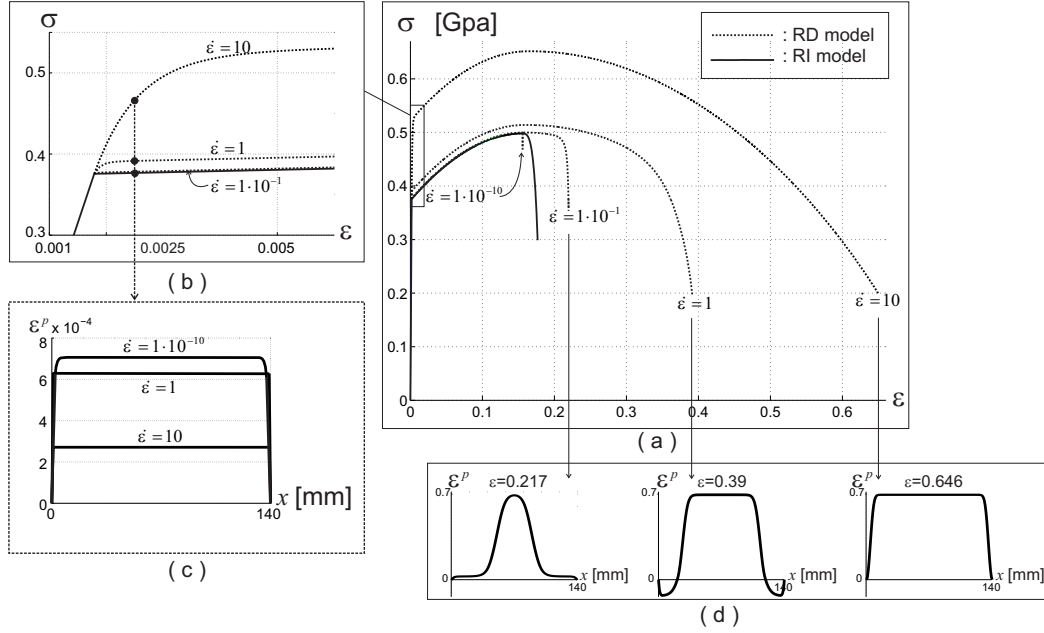


Figure 15: (a) $\sigma - \epsilon$ response at high deformation rates. (b) Enlargement at the onset of the hardening plastic phase. (c) Profiles of ϵ^p at $\epsilon = 0.0025$, for different deformation rates. (d) Profiles of ϵ^p at fracture. $\dot{\epsilon} = [\text{s}^{-1}]$.

A_2 A_3 representing the gray areas of Fig. 13(c). On the other hand in Fig. 11 the displacement $\Delta s = \int_{x_1}^{x_2} u' dx$ is considered in comparison to experimental curve. Accordingly, the elongation is registered as $\Delta s_b - \Delta s_a = A_1 - 2A_2 = 2.12$ mm (see Fig. 13(c)) in the softening phase. In this case, strain recovery is taken into account only partially, because the shortening occurring outside the measurement basis (x_1 , x_2), equal to the area $2A_3$ in Fig. 13(c), is not taken into account. As a result, the slope of the softening branches of Fig. 11 is much smaller. The incremental ratio $\delta\epsilon^p/\delta\epsilon$ just before fracture are reported in Fig. 14. Much higher local strain rates are reached in the RD model case, since the softening phase occurs much faster in the RD model than in the RI model.

High deformation rates are considered in Fig. 15 ($\dot{\epsilon} = 0.1, 1$, and 10 s^{-1}). As the deformation rate increases, the behavior becomes stiffer, larger maximum stresses are obtained, and the softening branches extends. Fig. 15(c) shows the delay in the evolution of the plastic deformation encountered when high deformation rates are considered, i.e. when the deformation is dominated by the elastic strain. Plastic deformation localization is delayed or even smoothed out at high rates, as clearly shown in Fig. 15(d), where profiles of ϵ^p at fracture are plotted for different deformation rates. The zone where ϵ^p reaches the limit value of 0.7 is larger and larger as $\dot{\epsilon}$ increases. For $\dot{\epsilon} = 10 \text{ s}^{-1}$, practically the whole bar attains the value $\epsilon^p = 0.7$, with the exception of short boundary layers. Note that, for $\dot{\epsilon} = 1 \text{ s}^{-1}$, plastic unloading outside the localization zone results in negative values of ϵ^p (local compression). The large deformation rates might not look realistic for this example as they are only considered to explore the different behaviors that the model is capable of describing.

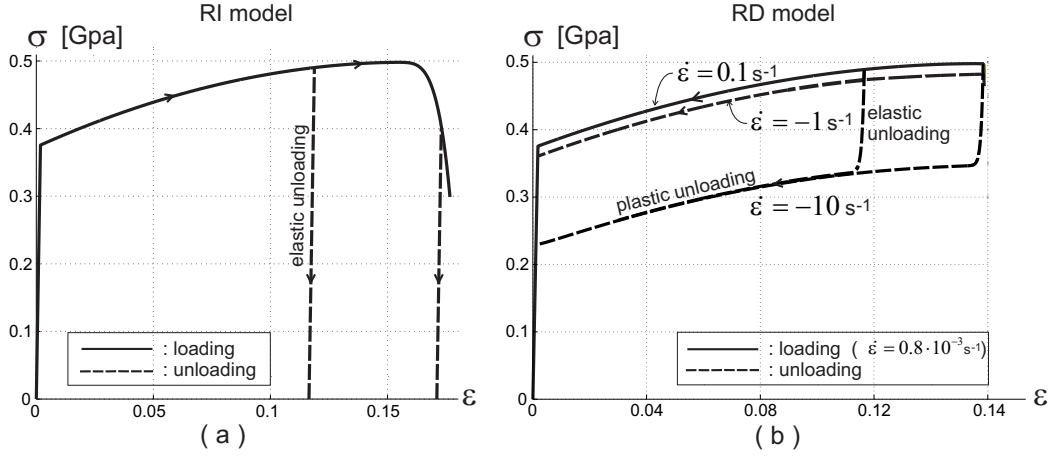


Figure 16: Loading (solid line) and unloading (dashed line) response curves: (a) RI model, (b) RD model.

In Figs. 16, and 17, the stress vs. strain response during unloading is analyzed. For the RI model, unloading is always elastic (Fig. 16(a)). For the RD model, unloading behavior depends on the deformation rate. For large negative deformation rates, hysteretic loops are obtained (Fig. 16(b)), where the area of the resulting closed curves represents the dissipated plastic energy. The unloading process exhibits two phases: in the first only elastic deformation reduces (elastic unloading), and it corresponds to the initial sloped branches of the $\sigma - \epsilon$ curves of Fig. 16(b). In the second phase, plastic unloading occurs, and the corresponding $\sigma - \epsilon$ branch is parallel to the loading curve. Since dissipation is related to the viscous stress (6), it increases with increasing $|\dot{\epsilon}|$. For deformation rates lower than 0.1 s^{-1} , dissipation practically disappears, and the loading and unloading curves are coincident. Exceptions are found when low deformation rates are applied and unloading is started from points belonging to the softening branch, as shown in Fig. 17. In this situation, small unloading rates cannot stop and invert the process of strain localization, developed in the softening regime, and, thus, localization proceeds up to failure. Stress-strain curves for different deformation rates are plotted in Fig. 17(a,b), and profiles of ϵ^p at different deformation states are presented in Fig. 17(c) for $\dot{\epsilon} = -0.01 \text{ s}^{-1}$.

Fig. 18 deals with the relaxation problem solved by the RD model. Relaxation from different states of the deformation process obtained with $\dot{\epsilon} = 1 \text{ s}^{-1}$ is analyzed. The $\sigma - \epsilon$ curve corresponding to $\dot{\epsilon} = 1 \text{ s}^{-1}$ is plotted in Fig. 18(a). The bar relaxes in two possible ways. (i) If relaxation is conducted from states characterized by a value of ϵ smaller than 0.156, which is the transition from a steady states process to localization, then ϵ^p evolves toward the corresponding steady state configuration. An example regarding this situation is presented in Fig. 18(b). Keeping $\epsilon = 0.15$ fixed, the starting ($t = 0$) and ending ($t = 10000 \text{ s}$) configurations of the relaxation process are demonstrated. (ii) If the bar is relaxed from states with ϵ larger than 0.156, then the process develops to fracture. This kind of process is depicted in Fig. 18(c). For $\epsilon = 0.25$, the deformation localizes and very quickly terminates in final fracture at $t = 0.26 \text{ s}$.

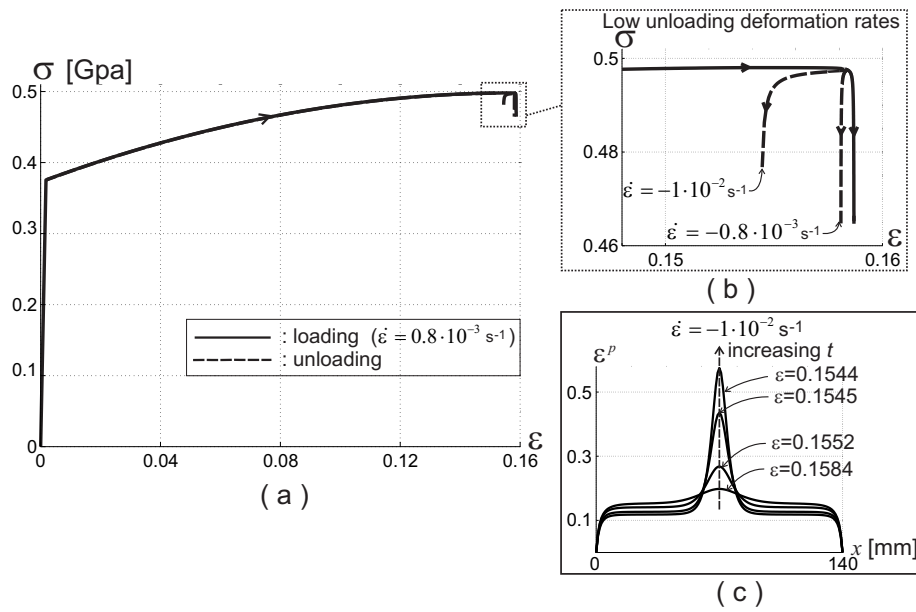


Figure 17: Unloading with RD model at low deformation rates starting from softening states: (a-b) response curves, (c) evolution of ϵ^p .

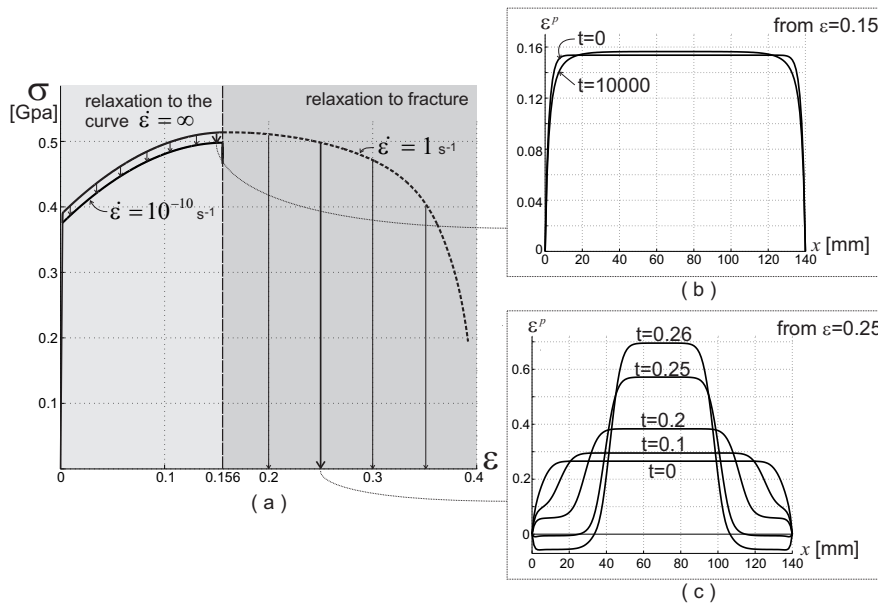


Figure 18: (a) Relaxation at $\dot{\epsilon} = 1 \text{ s}^{-1}$. (b) Evolution of the relaxation process at $\epsilon = 0.15$ and (c) at $\epsilon = 0.25$.

6. Concluding remarks and perspectives

A simple demonstration of the influence of plastic energy potential on the inhomogeneous distribution of the strain field, strain localization and necking is presented through two non-local plasticity models. **The first model is a rate-dependent one accounting for partially recoverable and viscously dissipated plastic deformation. The other one is a rate-independent model, which accounts for totally dissipative plastic deformation.** Both plasticity models are enhanced by a gradient energy and a non-convex plastic potential contribution. The first contribution introduces a length parameter into the model allowing studies at different length scales and the second one introduces an instability leading to decomposition or localization of the plastic strain. The instability due to the second contribution is stabilized by the gradient energy function. The numerical examples illustrate good agreement between the models where they naturally capture the evolution of deformation patterns and localization. In both the models, the non-convexity of the plastic potential drives the strain localization. At the onset of localization, the small disturbances inherent the numerical algorithm are sufficient to select a solution when multiple solutions are possible, and any external additional assumption, such as initial defects in the material or geometrical inhomogeneities, is unnecessary to trigger localization. At low deformation rates the results of the rate-dependent model approach those of the rate-independent model. Both models have exhibited a great versatility in modeling different plastic processes, depending on the form assigned to the plastic potential. Indeed, the convexity-concavity properties strongly influence the evolution of the plastic deformation: a convex energy leads to diffuse plastic deformations, while a concave energy produces localization. In the proposed simulations a double-well and a convex-concave potential has been proposed to reproduce plastic processes at meso and macro scales, and their shape has been fixed by phenomenological fits to experimental data. The study of physics-based correlations between the plastic energy and material properties represents an interesting challenge for future work, requiring multidisciplinary efforts (solid-state physics, material chemistry, micro-mechanics, etc.). Differences between the two models have been highlighted. In the rate-dependent model, the viscous nature of the plastic dissipation describes the delay or, eventual, annihilation of the strain localization, at large deformation rates. It also allows the phenomena of relaxation to be described. This character is obviously absent in the rate-independent model. **The fact that the plastic energy is stored and dissipative in the rate-dependent and rate-independent model, respectively, results in completely different predictions during unloading, as shown in Sect. 5. The rate-independent model accounts for elastic unloading, as observed in tensile tests on steel bars, while the rate-dependent model describes plastic unloading, with the exception of a plastic deformation portion dissipated by viscosity.** The current models have however been primarily developed to capture localization under monotonic loading. Further work is required to fully explore the most appropriate form of model to capture the full range of observed phenomena during unloading or relaxation from a pre-deformed state.

Acknowledgements

Tuncay Yalçinkaya greatly acknowledges financial support for this work provided by TUBITAK (The Scientific and Technological Research Council of Turkey) within the project 112C023 through 2236 Co-Circulation Scheme supported by the EC-FP7 Marie Curie Actions.

Giovanni Lancioni was partially supported by the Italian Ministry of Education, Universities and Research (MIUR) by the PRIN funded Program “Dynamics, stability and control of flexible structures”, 2010/11N. 2010MBJK5B.

References

- Alessi, R., Marigo, J., Vidoli, S., 2015. Gradient damage models coupled with plasticity: variational formulation and main properties. *Mechanics of Materials* 80, 351–367.
- Amor, H., Marigo, J., Maurini, C., 2009. Regularized formulation of the variational brittle fracture with unilateral contact: numerical experiments. *J. Mech. Phys. Solids* 57, 1209–1229.
- Bayley, C. J., Brekelmans, W. A. M., Geers, M. G. D., 2006. A comparison of dislocation induced back stress formulations in strain gradient crystal plasticity. *International Journal of Solids and Structures* 43, 7268–7286.
- Bourdin, B., Francfort, G., Marigo, J., 2000. Numerical experiments in revisited brittle fracture. *J. Mech. Phys. Solids* 48, 797–826.
- Carstensen, C., Hackl, K., Mielke, A., 2002. Non-convex potentials and microstructures in finite-strain plasticity. *Proc. R. Soc. A* 458, 299–317.
- de Borst, R., 1987. Computation of post-bifurcation and post-failure behaviour of strain-softening solids. *Computers & Structures* 25, 211–224.
- de Borst, R., Pamin, J., Peerlings, R., Sluys, L., 1995. On gradient-enhanced damage and plasticity models for failure in quasi-brittle and frictional materials. *Comput. Mech.* 17, 130–141.
- Del Piero, G., 2013. A variational approach to fracture and other inelastic phenomena. *J. Elast.* 112(1), 3–77.
- Del Piero, G., Lancioni, G., March, R., 2007. A variational model for fracture mechanics: numerical experiments. *J. Mech. Phys. Solids* 55, 2513–2537.
- Del Piero, G., Lancioni, G., March, R., 2013. A diffuse cohesive energy approach to fracture and plasticity: the one-dimensional case. *Journal of Mechanics of Materials and Structures* 8(2-4), 109–151.
- Freddi, F., Royer-Carfagni, G., 2010. Regularized variational theories of fracture: a unified approach. *J. Mech. Phys. Solids* 58, 1154–1174.
- Gill, P., Murray, W., Wright, M., 1981. *Practical optimization*. Academic Press.
- Gudmundson, P., 2004. A unified treatment of strain gradient plasticity. *J. Mech. Phys. Solids* 52, 1379–1406.
- Gurtin, M., Anand, L., 2005. A theory of strain-gradient plasticity for isotropic, plastically irrotational materials. part i: Small deformations. *J. Mech. Phys. Solids* 53, 1624–1649.
- Gurtin, M., Anand, L., 2009. Thermodynamics applied to gradient theories involving the accumulated plastic strain: the theories of aifantis and fleck & hutchinson and their generalization. *J. Mech. Phys. Solids* 57, 405–421.
- Gurtin, M. E., 2000. On the plasticity of single crystals: free energy, microforces, plastic-strain gradients. *J. Mech. Phys. Solids* 48, 989–1036.
- Gurtin, M. E., 2002. A gradient theory of single-crystal viscoplasticity that accounts for geometrically necessary dislocations. *J. Mech. Phys. Solids* 50, 5–32.
- Jirásek, M., Rolshoven, S., 2009a. Localization properties of strain-softening gradient plasticity models. part i: strain-gradient theories. *Int. J. Solids Structures* 46, 2225–2238.
- Jirásek, M., Rolshoven, S., 2009b. Localization properties of strain-softening gradient plasticity models. part ii: theories with gradients of internal variables. *Int. J. Solids Structures* 46, 2239–2254.
- Klusemann, B., Kochmann, D., 2014. Microstructural pattern formation in finite-deformation single-slip crystal plasticity under cyclic loading: Relaxation vs. gradient plasticity. *Comput. Methods in Appl. Mech. Eng.* 278, 765–793.
- Klusemann, B., Yalçinkaya, T., 2013. Plastic deformation induced microstructure evolution through gradient enhanced crystal plasticity based on a non-convex helmholtz energy. *International Journal of Plasticity* 48, 168–188.
- Klusemann, B., Yalçinkaya, T., Geers, M. G. D., Svendsen, B., 2013. Application of non-convex rate dependent gradient plasticity to the modeling and simulation of inelastic microstructure development and inhomogeneous material behavior. *Computational Materials Science* 80, 51–60.
- Lancioni, G., 2015. Modeling the response of tensile steel bars by means of incremental energy minimization. *J. Elasticity*, online, DOI 10.1007/s10659-015-9515-8.

- Lancioni, G., Royer-Carfagni, G., 2009. The variational approach to fracture mechanics. a practical application to the french panthéon in paris. *J. Elast.* 95, 1–30.
- Lancioni, G., Yalcinkaya, T., 2014. Plastic slip patterns through rate-independent and rate-dependent plasticity. *Key Engineering Materials* 611-612, 1777–1786.
- Lancioni, G., Zitti, G., Yalcinkaya, T., 2015. Rate-independent deformation patterning in crystal plasticity. *Key Engineering Materials, Proceeding ESAFORM2015*.
- Miehe, C., Lambrecht, M., 2003a. Analysis of microstructure development in shearbands by energy relaxation of incremental stress potentials: Large-strain theory for standard dissipative solids. *International Journal for Numerical Methods in Engineering* 58, 1–41.
- Miehe, C., Lambrecht, M., 2003b. A two-scale finite element relaxation analysis of shear bands in non-convex inelastic solids: small-strain theory for standard dissipative materials. *Comput. Methods in Appl. Mech. Eng.* 192, 472–508.
- Miehe, C., Lambrecht, M., Gurses, E., 2004. Analysis of material instabilities in inelastic solids by incremental energy minimization and relaxation methods: evolving deformation microstructures in finite plasticity. *J. Mech. Phys. Solids* 52, 2725-2769.
- Mielke, A., 2005. Evolution of rate-independent systems. *Handbook of Differential Equations: Evolutionary Equations, North-Holland* 2, 461–559.
- Nguyen, Q., 2000. *Stability and nonlinear solid mechanics*. JOHN WILEY & SONS, LTD.
- Ortiz, M., Repetto, E. A., 1999. Nonconvex energy minimization and dislocation structures in ductile single crystals. *J. Mech. Phys. Solids* 47, 397–462.
- Pham, K., Amor, H., Marigo, J., Maurini, C., 2011. Gradient damage models and their use to approximate brittle fracture. *Int. J. Damage Mech.* 20, 618–652.
- Pham, K., Marigo, J., 2013. From the onset of damage until the rupture: construction of the responses with damage localization for a general class of gradient damage models. *Continuum Mech. Thermodyn.* 25(2-4), 147–171.
- Sun, H. B., Yoshida, F., Ma, X., Kamei, T., Ohmori, M., 2003. Finite element simulation on the propagation of Lüders band and effect of stress concentration. *Materials Letters* 57, 3206–3210.
- Yalcinkaya, T., Brekelmans, W. A. M., Geers, M. G. D., 2012. Non-convex rate dependent strain gradient crystal plasticity and deformation patterning. *International Journal of Solids and Structures* 49, 2625–2636.
- Yalcinkaya, T., 2013. Multi-scale modeling of microstructure evolution induced anisotropy in metals. *Key Engineering Materials* 554-557, 2388–2399.
- Yalcinkaya, T., Brekelmans, W. A. M., Geers, M. G. D., 2009. A composite dislocation cell model to describe strain path change effects in BCC metals. *Model. Simul. Mater. Sci. Eng.* 17, 064008.
- Yalcinkaya, T., Brekelmans, W. A. M., Geers, M. G. D., 2011. Deformation patterning driven by rate dependent nonconvex strain gradient plasticity. *Journal of the Mechanics and Physics of Solids* 59, 1–17.
- Yalcinkaya, T., Lancioni, G., 2014. Energy-based modeling of localization and necking in plasticity. *Procedia Materials Science* 3, 1618–1625.
- Yoshida, F., Kaneda, Y., Yamamoto, S., 2008. A plasticity model describing yield-point phenomena of steels and its application to fe simulation of temper rolling. *International Journal of Plasticity* 24, 1792-1818.